Fillet Weld Effective Lengths in CHS X-Connections. II: Finite Element Modelling, Parametric Study and Design

Kyle Tousignant[a] and Jeffrey A. Packer[a*]

[a] Department of Civil Engineering, University of Toronto, 35 St. George Street, Toronto, ON, M5S 1A4, Canada

[*] Corresponding Author. E-mail: jeffrey.packer@utoronto.ca; Tel: +1-416-978-4776; Fax: +1-416-978-7046

Abstract

Finite element (FE) modelling was performed to extend the results of a recently completed experimental test program to evaluate the static strength of fillet welds in X-connections between circular hollow sections (CHS). Non-linear FE models with weld fracture were validated by comparison of spot strains, load-deformation response, and fracture load with 12 experimental tests. Two hundred and fifty-six FE weld-critical CHS-to-CHS X-connections, with varied branch-to-chord diameter ratio, chord wall slenderness, branch inclination angle, and branch-to-chord thickness ratio, were analysed under quasi-static branch tension. The effect of these parameters on fillet weld strength is illustrated, and the structural reliability (or safety index) of North American specification provisions for weld effective lengths is confirmed. An alternative method for estimating fillet weld strength, with specific weld effective lengths, is proposed. Recommendations for a new design approach that meets the minimum target safety index in North America are made.

Key words

Circular hollow section, Fillet weld, Effective length, Connection, Parametric study, Finite element

1. Introduction

To date, only one experimental study has been conducted to evaluate the performance of welds in hollow structural section (HSS) connections to a circular hollow section (CHS) chord [1]. Without experimental evidence, specifications have been reluctant to provide a "fit-for-purpose" approach to weld design that takes into account the non-uniform contribution of the weld perimeter by using weld effective lengths. Currently, only AWS D1.1 "Structural Welding Code – Steel" [2] gives such a method, in Clause 9.6.1.3(4), but it is badly defined. Instead, welds in connections to a CHS chord are routinely sized to develop the yield capacity of the connected branch member. This is done by meeting prescriptive requirements for the weld throat dimension (t_w) as a function of the branch thickness (t_b). In rare cases, it is suggested that welds be designed for the connection capacity, instead of the yield capacity of the branch [2]. According to ISO [3], this approach is not common.

In the lone experimental study that evaluated the performance of welds in CHS-to-CHS X-connections (Fig. 1), linear strain gauge (SG) measurements adjacent to the weld showed that load transfer was highly non-uniform, and peaked in the saddle position. This indicates that a weld effective length phenomenon exists in CHS connections. A reliability analysis of the experimental results determined that the weld effective length provisions given by Clause 9.6.1.3(4) of AWS [2] are highly conservative. For the range of parameters studied, the AWS [2], AISC [4], and CSA [5] provisions for fillet weld design exceeded the minimum safety index in North America ($\beta^+ > 4.0$), even without weld effective lengths [1].

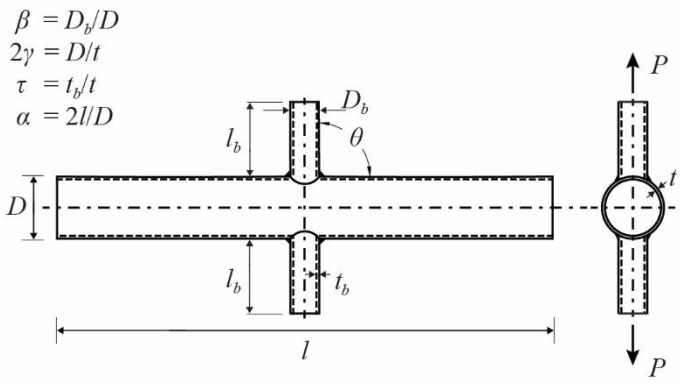

Fig. 1. CHS X-connection general configuration and non-dimensional parameters

This paper presents a parametric modelling study that was performed, using finite element (FE) methods, to determine: (a) the effect of key connection parameters on weld strength in CHS X-connections; (b) if these findings

are applicable to a wider range of fillet-welded CHS X-connections; and (c) a better method for estimating fillet weld strength, using weld effective lengths.

2. Fillet Weld Design for CHS X-Connections

2.1. AWS D1.1-15

The definitive guidance on weld design for CHS-to-CHS connections in North America is given by AWS D1.1 [2]. AWS uses the term "T-, Y-, and K-connections" generically to describe welded connections between CHS, and also refers to X-connections as double-tee connections (Clause 9.6.1.5). For such connections, AWS D1.1 Clause 9.6.1.3 points out that "…due to differences in the relative flexibilities of the main member loaded normal to its surface, and the branch member carrying membrane stresses parallel to its surface, transfer of load across the weld is highly non-uniform, and local yielding can be expected before the connection reaches its design load". AWS gives two possible methods to proportion fillet welds in CHS connections: a fit-for-purpose approach, using a weld effective length, and a prequalified weld size approach.

2.1.1. Weld effective length design approach

AWS [2] Clause 9.5.3 permits the nominal strength (P_n) of fillet welds to be calculated according to Eqs. (1) and (2):

$$P_n = Q_w l_e \tag{1}$$

$$Q_w = 0.60 t_w F_{EXX} \tag{2}$$

where l_e = weld effective length, and F_{EXX} = ultimate strength of weld metal (a minimum specified tensile strength is used). An LRFD resistance factor for fillet welds, ϕ, equal to 0.80, is then applied to determine the design strength of the fillet weld (ϕP_n).

Equations for the total weld length (l_w) are given in AWS [2] Clause 9.5.4, in the following form:

$$l_w = \pi D_b K_a \tag{3}$$

where D_b = diameter of the CHS branch, and K_a = weld length factor, giving the ratio of the total weld length (taken along the weld root) to the branch circumference. The simplest K_a factor used by AWS is:

$$K_a = \frac{1 + 1/\sin\theta}{2} \tag{4}$$

where θ = branch inclination angle.

The effective weld length (l_e) in AWS [2] is implied by a branch stress/load factor of 1.5 specified in Clause 9.6.1.3(4), for LRFD, which is stated to "… account for non-uniform distribution of load". The inverse of this factor gives l_e as a fraction of the total weld length (l_w):

$$l_e = \frac{2}{3} l_w \tag{5}$$

2.1.2. Prequalified fillet weld design approach

AWS [2] Clause 9.6.1.3(3) states that if prequalified fillet weld details are used per their Figure 9.10, and CHS have a yield strength (F_y) > 280 MPa, then t_w may be specified as the lesser of Eqs. (6) and (7):

To develop the capacity of the connected member walls:

$$t_w = 1.07 t_b \tag{6}$$

To develop the local "punching shear" connection capacity of the chord:

$$t_w = t \tag{7}$$

where t = CHS chord thickness.

AWS [2] Figure 9.10 provides dimensions for equal weld legs ($l_v = l_h$) that satisfy either Eq. (6) or Eq. (7). These dimensions are subject to the following limitations: $\beta \leq 0.33$ (per Clause 9.5.1.2); local dihedral angle (Ψ) such that $30° \leq \Psi \leq 120°$. Furthermore, when $\Psi < 60°$ the Z loss values in AWS [2] Table 9.5, for PJP welds, must be applied (Note 4 in Figure 9.10 of AWS [2]). These limitations ensure that the leg dimensions given in AWS [2] Figure 9.10 produce the throat size intended by Eq. (6) or Eq. (7).

2.2. Prequalified fillet weld design approach according to CIDECT

The CIDECT design guide for statically loaded CHS connections [6] gives a prequalified fillet weld design approach based on the Directional Method of EN 1993-1-8 [7]. By setting the weld resistance equal to the design capacity of the branch, $t_w = 1.10 t_b$ is given to develop the capacity of the connected member walls for steel with F_y = 355 MPa. This is determined by assuming a 90° branch welded to a flat surface, and a weld effective length equal to πD_b (i.e. $l_e = l_w$).

Fleischer & Herion [8] aimed to reduce the prequalified weld throat from $t_w = 1.10t_b$ by taking into account the actual weld length in CHS connections. The actual weld length is a function of the branch inclination angle (θ) and the branch-to-chord diameter ratio ($\beta = D_b/D$) (Fig. 1). To take the actual weld length into account, the authors borrowed a more accurate K_a value from AWS [2] Clause 9.5.4. They then computed the weld strength using the Simplified Method of EN1993-1-8 [7], which is a conservative (lower-bound) design alternative to the Directional Method. It is easier to apply to CHS connections because it does not require stress components on the throat plane to be determined. Using the CIDECT methodology (i.e. setting weld strength equal to branch capacity), it was shown that the prequalified fillet weld size could theoretically be reduced for some joints. The required fillet weld throat was a complex function of β, the branch slenderness ratio (D_b/t_b), and θ (Fig. 1). Design charts were hence given for simplicity. This work was still based on the design philosophy of developing the capacity of the connected member walls. Moreover, weld effective lengths were not determined.

2.3. Caulkins [9] and Marshall [10]

Caulkins [9] did work relevant to a fit-for-purpose approach to weld design for CHS connections. He showed, using a shell theory solution, that load transfer through the weld peaks at the saddle points in CHS-to-CHS T-connections. Recent experimental research has confirmed this for CHS-to-CHS X-connections [1]. Marshall [10] used the same data to demonstrate that load transfer efficiency is greater for T-connections with low D/t (i.e. a stocky chord member), low β, and low branch-to-chord thickness (τ) (Fig. 2). In his attempt to generalize the results, he found that evidence on the effect of high β was mixed.

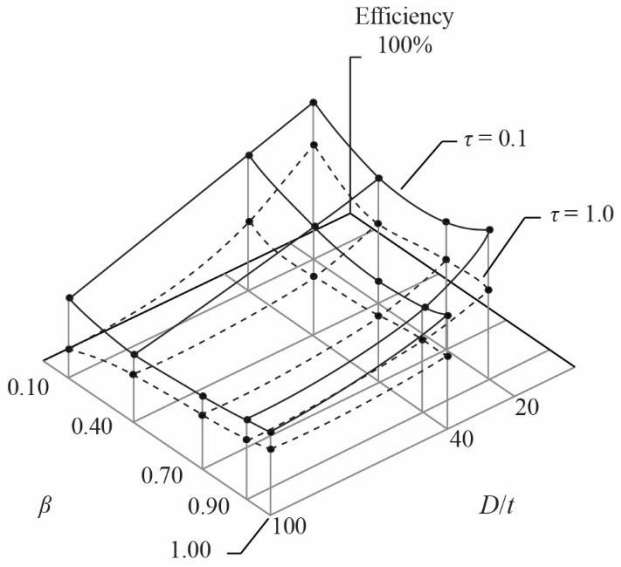

Fig. 2. Load transfer efficiency across the weld of a 90° CHS-to-CHS T-connection (adapted from Marshall [10])

In the work by Caulkins [9] and Marshall [10], load transfer efficiency was defined as the ratio of nominal-to-peak elastic load at the connection. This ratio was believed to be related to the weld effective length. In another study by Wang et al. [11], load transfer efficiency was defined as the ratio of nominal-to-peak elastic strain measured adjacent to the weld. This study investigated weld effective lengths for connections between CHS branches and rectangular hollow section (RHS) chords. The definition of load transfer efficiency is marginally different, but the methods provide the same results because load and strain are linearly related in the elastic range. Tousignant & Packer [1] showed that these methods provide a very conservative lower-bound when used to explicitly determine l_e.

3. Finite element modelling

To validate the FE modelling approach used herein, 12 CHS-to-CHS X-connections were developed to replicate previous experimental tests, with the same geometric and material properties as the experimental specimens [1]. The geometric properties and experimental results are summarized in Table 1.

Table 1

Geometric properties of 12 CHS X- (test) connections and comparison of experimental and FE results

Test	θ	CHS branch member $D_b \times t_b$	CHS chord member $D \times t$	t_w	P_a [a]	P_a' [b]	δ_a [c]	P_{FE} [d]	δ_{FE} [d]	P_a'/P_{FE}	δ_a/δ_{FE}
	°	mm × mm	mm × mm	mm	kN	kN	%	kN	%		
102-273-90a	90	102.0 × 7.34	273.5 × 11.69	4.08	672	672	3.23	655	2.72	1.03	1.19
102-273-90b		102.0 × 7.34	273.5 × 11.69	4.37	678	678	3.68	690	3.03	0.98	1.21
102-406-90a		102.0 × 7.34	406.5 × 12.34	3.56	608	608	4.70	543	3.31	1.12	1.42
102-406-90b		102.0 × 7.34	406.5 × 12.34	3.14	540	540	3.52	495	2.87	1.09	1.23
127-273-90a		127.4 × 11.55	273.5 × 11.69	3.63	653	653	2.06	762	2.67	0.86	0.77
127-273-90b		127.4 × 11.55	273.5 × 11.69	4.00	609	653	2.07	811	2.98	0.80	0.69
127-406-90a		127.4 × 11.55	406.5 × 12.34	3.16	557	557	2.61	631	3.21	0.88	0.81
127-406-90b		127.4 × 11.55	406.5 × 12.34	3.47	556	557	2.78	617	3.01	0.90	0.92
102-406-60a	60	102.0 × 7.34	410.0 × 12.21	3.58	721	721	3.34	640	2.62	1.13	1.28
102-406-60b		102.0 × 7.34	410.0 × 12.21	3.79	538	721	3.63	672	2.84	1.07	1.28
127-406-60a		127.4 × 11.55	410.0 × 12.21	3.95	761	761	2.34	903	3.58	0.84	0.65
127-406-60b		127.4 × 11.55	410.0 × 12.21	3.38	798	850	3.60	798	2.87	1.06	1.25

[a] Actual (experimental) weld fracture load.

[b] Greatest load sustained by the weld.

[c] Actual (experimental) chord deformation at weld fracture (as % of measured CHS chord dimeter D) averaged over both branches.

[d] P_{FE} and δ_{FE} are analogous to P_a' and δ_a, but refer to the FE values at weld fracture.

The 12 connections were modelled using the commercially available software package ANSYS 14.0 [12]. Although it was possible to model just one eighth of the non-inclined ($\theta = 90°$) connections due to symmetry about three principal planes passing through the connection work point, one half of each connection was modelled instead, for all connections, to accommodate the inclined branch cases. This simplified the parametric programming of the models, which was later done using ANSYS batch files. Symmetry boundary conditions were applied in the plane of the connection (i.e. along the cut face). To replicate the experimental connection of the branches to the chord, a 0.25-mm gap was modelled between the two members. This gap ensured that the applied load was only transferred through the fillet weld (i.e. it prevented direct load transfer between the branch and chord members). The value of 0.25 mm (which is close to the Boolean tolerance of the FE program) was selected to minimize the effect of the gap on the relationship between l_v, l_h, and t_w at any point along the weld length. The general connection geometry (showing the gap), mesh layout, and boundary conditions are shown in Fig. 3 (for a non-inclined connection) and Fig. 4 (for an inclined connection).

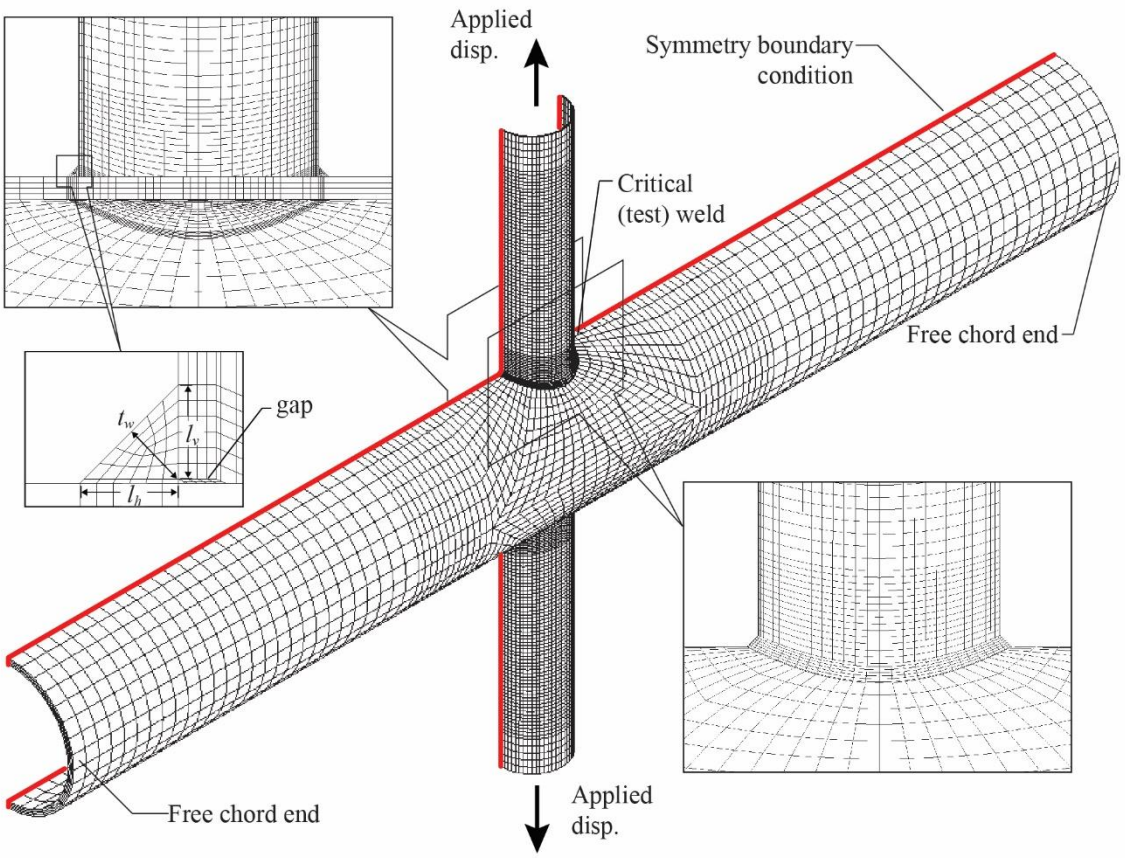

Fig. 3. FE CHS-to-CHS X-connection geometry, mesh layout, and boundary conditions with $\theta = 90°$

139

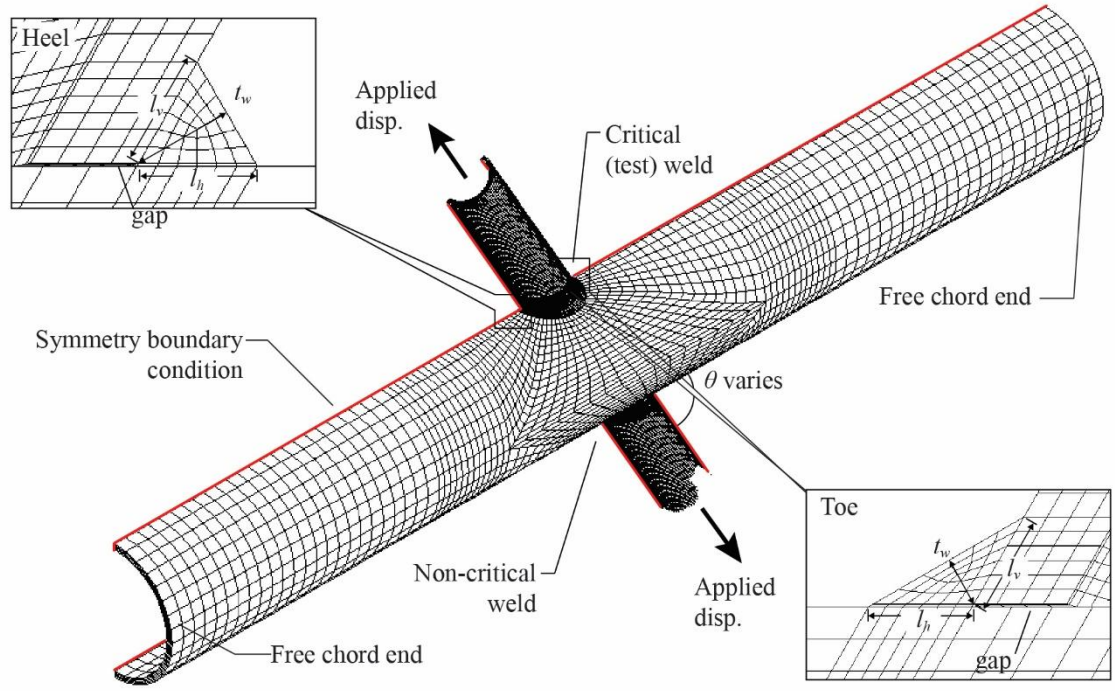

Fig. 4. FE CHS-to-CHS X-connection geometry, mesh layout, and boundary conditions with $\theta < 90°$ ($\theta = 60°$ shown)

All FE analyses were conducted by applying static incremental displacements (non-linear time-step analysis) to the ends of the specimen (e.g. the ends of each branch, or for coupon tests, the ends of each coupon). Large deformation allowance (non-linear geometry) and non-linear material properties (for each different material) were included.

3.1. Material properties

Multi-linear true stress-strain curves for each different material (i.e. the weld metal, and each different branch and chord member) were derived from tensile coupon tests conducted in accordance with ASTM A370 [13]. The procedure used is as follows:

1. Prior to necking: the average engineering stress (σ) and engineering strain (ε) ordinates from the tests were converted to true stress (σ_T) and true strain (ε_T). The following well-known relationships were used [14]:

$$\sigma_T = \sigma(1 + \varepsilon) \tag{8}$$

$$\varepsilon_T = ln(1 + \varepsilon) \tag{9}$$

2. After necking: an iterative approach based on weighting an approximate lower- and upper-bound to the true stress versus true strain response was used to determine the ordinates on the curve:

$$\sigma_T = \sigma_T' \left[w(1 + \varepsilon_T - \varepsilon_T') + (1 - w) \left(\frac{\varepsilon_T^{\varepsilon_T'}}{\varepsilon_T'^{\varepsilon_T'}} \right) \right] \tag{10}$$

where σ_T' = true stress at the start of necking, ε_T' = true strain at the start of necking, and w = weighting factor [15].

The weighting factor in Eq. (10) was derived for each different material by matching the engineering stress-strain curve of a tensile coupon modelled in ANSYS to the average engineering stress-strain curve from the experimental tests. The FE coupon was modelled using the average measured geometry from the tests, with the original curved shape for CHS coupons. The engineering strains for the FE coupons were calculated over a 50-mm gauge length from nodes on the exterior of the coupon to closely mimic the experimental method using a clip gauge. Typical engineering stress-strain curves and the corresponding true stress-strain curves derived using the above process are shown in Figs. 5a,b. In Figs. 5a,b the solid line is the average experimental curve and the dashed line is

the FE-generated curve. The true stress-strain curves continue indefinitely along the x-axis since a fracture criterion was not calibrated for the coupons. Material properties for the 12 X-connections are given in Tousignant & Packer [1].

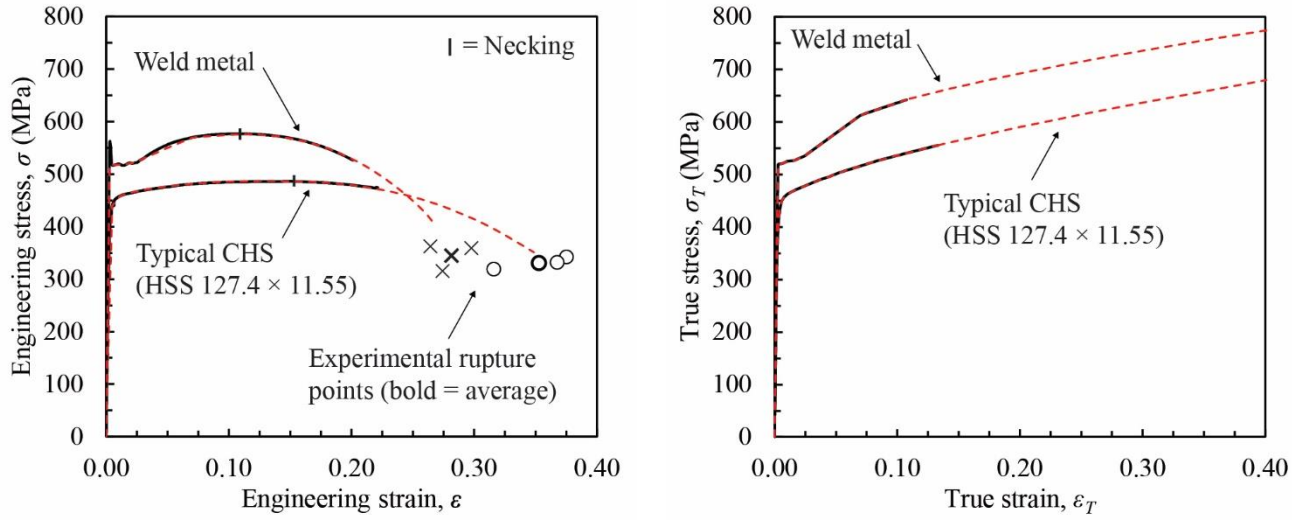

(a) Engineering stress-strain

(b) True stress-strain

Fig. 5. Comparison of typical experimental (solid line) and FE (dashed line) stress-strain curves

During the experimental tensile coupon tests, it was necessary to remove the clip gauge shortly after necking to prevent damage to it. The comparison of the FE and experimental engineering stress-strain curves therefore involved the pre-necked portion and a small variable amount of the post-necked portion of the curve, and the ordinates at rupture (shown with 'x' and 'o' markers in Fig. 5a). The engineering rupture stress was determined by dividing the load just before rupture by the initial cross-sectional area of the coupon, and the rupture strain was determined by rejoining the fractured coupon, measuring it to determine the final gauge length, and dividing the final gauge length by the initial gauge length. At rupture, the necked shape of the FE coupons closely resembled that of the experimental coupons, with necking at the mid-point. The same elements ultimately used for the CHS X-connection models (eight-noded solid brick elements) were used.

3.2. Model sensitivity study

To determine the best-suited mesh layout and element type for the CHS X-connection models, a model sensitivity study was performed. Figs. 6a - c show the typical mesh layouts studied, which were adapted to 60° and

90° connections. The mesh layout in Fig. 6a has the same number of elements circumferentially around the branch as the mesh layout in Fig. 6b, but fewer elements on the chord adjacent to the weld. The mesh layout in Fig. 6c has more elements circumferentially around the branch than the mesh layouts in Figs. 6a,b, as well as more elements on the chord adjacent to the weld. Table 2 gives additional parameters for the meshes studied.

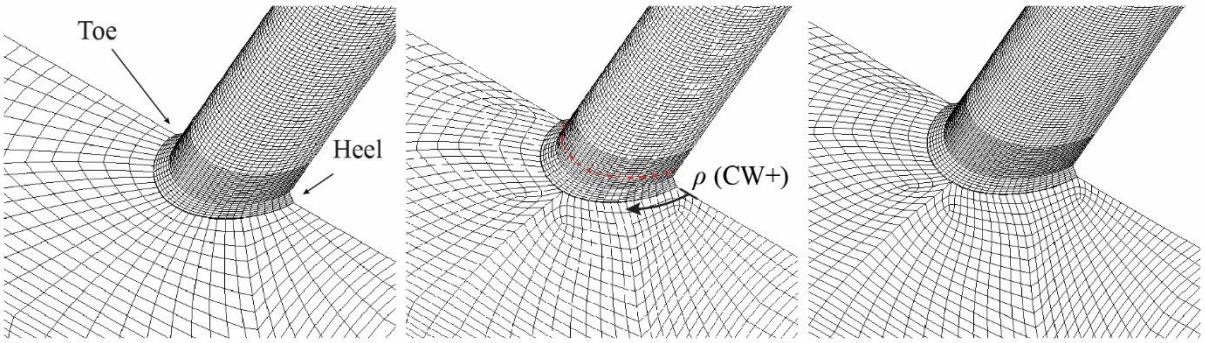

Fig. 6. Mesh layouts used in the mesh sensitivity study

Table 2

Mesh sensitivity study results for test 102-273-90a

Mesh layout	Element type	No. of elements	No. of nodes	CHS thickness elements	Weld face elements	k_{FE} kN/mm	k_a/k_{FE}	$P_{3\%D,FE}$ kN	$P_{3\%D,a}/P_{3\%D,FE}$
B	SOLID45	22520	33885	2	7	140.0	1.21	636	1.03
C	SOLID45[a]	33184	49863	2		139.8	1.21	634	1.03
B	SOLID45	32724	44520	3		157.2	1.08	663	0.99
B	SOLID95[b]	32724	165913	3	7	169.4	1.00	670	0.98
C	SOLID45	48456	65644	3		157.0	1.08	662	0.99
B	SOLID45	42928	55155	4		163.2	1.04	669	0.98
C	SOLID45	63728	81564	4	**7**	162.8	1.04	667	0.98
A	**SOLID45**	**36288**	**46685**	**4**		**166.6**	**1.01**	**677**	**0.97**

Note: k_a = 169.0 kN/mm and $P_{3\%D,a}$ = 654 kN.

The performance of each mesh layout and element type was evaluated by comparing the load-deformation response of the FE connection to the experimental test [1] (Fig. 7a). Table 2 compares the values of the initial stiffness (k_a = actual (experimental) initial stiffness, k_{FE} = FE initial stiffness) and the load at a chord deformation (δ) equal to 3%D (the connection plastification limit) [16] ($P_{3\%D,a}$ = actual load at connection plastification limit, $P_{3\%D,FE}$ = FE load at connection plastification limit). The value of δ was taken as the chord face deformation (normal to the chord, relative to the chord centre line) but averaged for both sides of the connection. Displacement was measured between points 50 mm away from the crown, as show in Fig. 7a. In general, as the number of nodes increased by using a finer mesh, a higher-order element, or more CHS through-thickness elements, the stiffness of the connection increased and so did the solution time. Fig. 7b demonstrates that the solution typically converged with four elements through the CHS thickness.

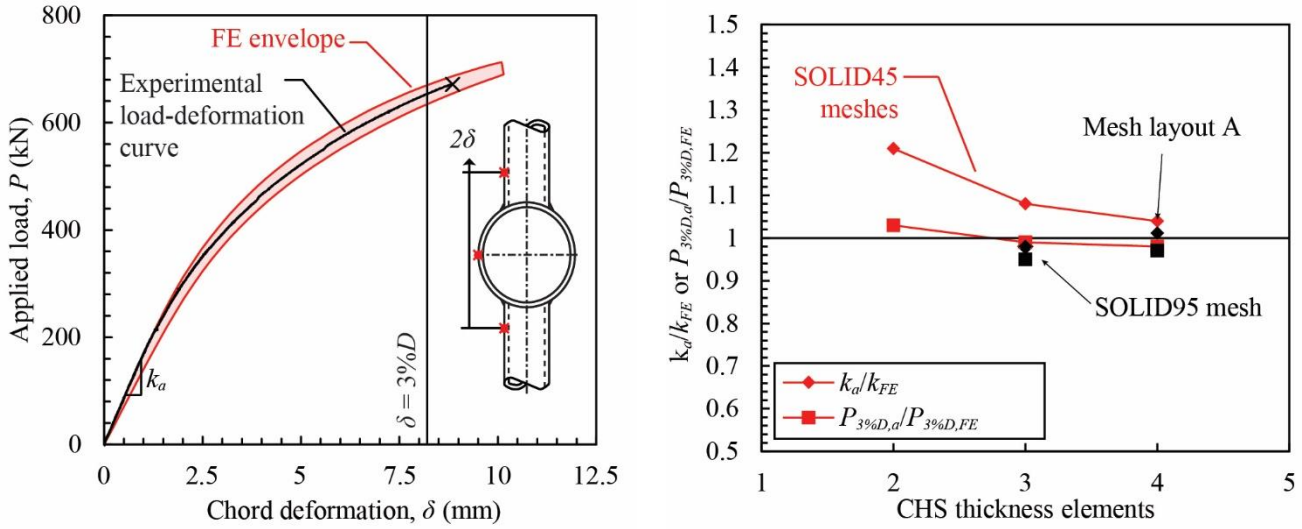

(a) load-deformation response

(b) FE convergence iterations

Fig. 7. Comparison of FE and experimental mesh sensitivity parameters for test 102-273-90a

The best overall agreement with the experimental results was obtained using a medium-density mesh (Mesh layout A or B), with four elements through the CHS branch and chord member thickness and eight-noded solid brick elements (SOLID45 in ANSYS). Elements used had reduced integration and hourglass control. To decide between Mesh layouts A and B, analyses of connections with different branch angles, β values, weld sizes, and CHS member thicknesses were undertaken to foresee any problems associated with these mesh types. Mesh layout A was found to be more capable of mapping to a wider range of connection geometries, and was therefore used.

3.2.1. Weld fracture criterion

An important part of the current study is modelling fillet weld fracture to determine the ultimate load for weld-critical connections. A method used in previous studies to model fracture in steel [17,18,19] was adopted herein. Fracture was modelled using the ANSYS element death feature, which was initiated by an equivalent strain fracture criterion (ε_{ef}). The ANSYS element death feature reduces the stress and stiffness of "killed" elements to near-zero, allowing the element to freely deform. The equivalent strain fracture criterion for the weld in the FE models was calibrated from six experimental tests (referred to as the "training set"), to match the load and chord deformation at weld fracture. Figs. 8a - c show the ratios of the actual (experimental) weld strength (taken as P_a', the maximum load experienced by the weld) to the FE rupture load (P_{FE}), and the ratio of the actual (experimental) deformation at rupture (δ_a) to the FE deformation at rupture (δ_{FE}), for the training set for different values of ε_{ef}. The curves are

spread over three plots for clarity. These figures illustrate that as ε_{ef} was increased, the ratios of experimental-to-FE load and deformation predictably decreased, because P_{FE} and δ_{FE} become greater. They also illustrate that connections with similar values of τ required similar values of ε_{ef} to obtain P_a'/P_{FE} and δ_a/δ_{FE} equal to 1 (i.e. to match the FE and experimental rupture loads and rupture deformations). To minimize error associated with this scatter, the average best-fit value over the six tests (ε_{ef} = 0.32) was selected as the fracture criterion. All 12 connections were then analysed using ε_{ef} = 0.32 for the fillet weld.

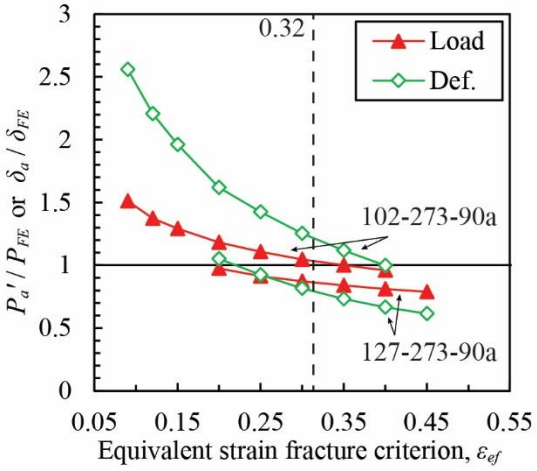

(a) tests 102-273-90a and 127-273-90a

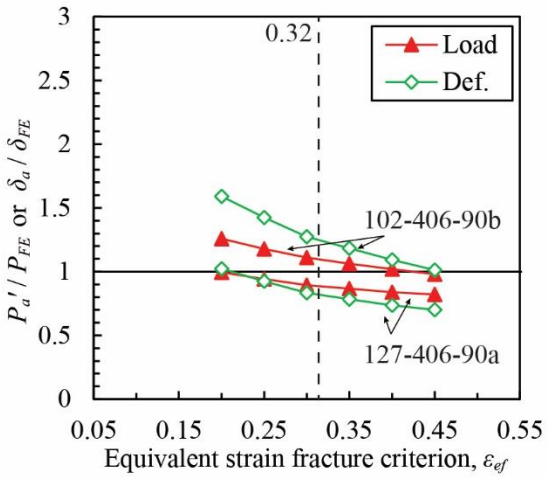

(b) tests 102-406-90b and 127-406-90a

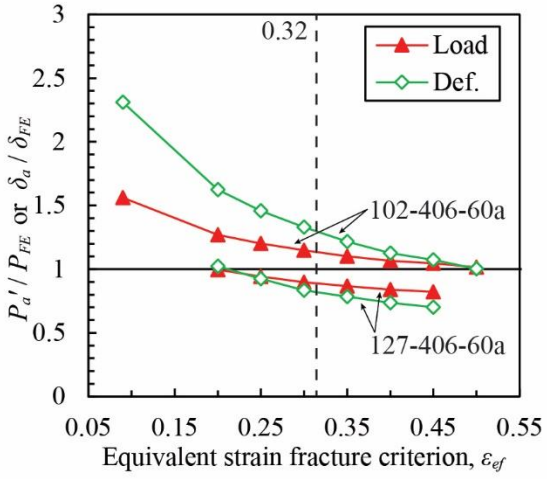

(c) tests 102-406-60a and 127-406-60a

Fig. 8. Ratios of P_a'/P_{FE} and δ_a/δ_{FE} for the training set for different values of ε_{ef}

3.2.2. Effect of model size (scalability)

The effect of absolute model size (e.g. using the same non-dimension parameters but different absolute values of the geometry) was investigated. The results of typical FE analyses are shown in Table 3. The same modelling techniques as above were used. The results in Table 3 indicate that the model and the weld strength are not sensitive to the absolute size of the model. Moreover, the normalized rupture load (P_{FE}/A_wF_{EXX}, where $A_w = t_w l_w$) is the same for models with the same non-dimensional parameters.

Table 3
Effect of model size

Branch diameter	Non-dimensional parameters				Weld dimensions			
	θ	β	D/t	τ	t_w	l_w	P_{FE}	P_{FE}/A_wF_{EXX}
mm	°				mm	mm	kN	
100	90	0.50	10	1.0	$0.50t_b$	320	1866	1.012
200	90	0.50	10	1.0	$0.50t_b$	639	7467	1.012
300	90	0.50	10	1.0	$0.50t_b$	959	16799	1.012
100	90	0.10	30	1.0	$0.50t_b$	314	3103	1.026
200	90	0.10	30	1.0	$0.50t_b$	629	12281	1.017

Note: all other geometry is calculated from the branch diameter, using the non-dimensional parameters shown.

4. Finite element models evaluated against experimental results

Figs. 9a,b compare the experimental and FE load-deformation curves for the six specimens in the training set. The deformations have been normalized, by dividing by D, so that curves for connections with different chord diameters can be presented on the same plot. For clarity, the six curves have been divided between two graphs. Chord deformations were measured as described in Section 3.2. Fig. 9 illustrates that the FE models are capable of predicting the actual response of the experiments. Figs. 10a,b show the correlation of the experimental and FE ultimate strengths and deformations (at rupture) for all 12 tests (see values in Table 1). The mean actual-to-FE predicted (A/P) rupture load was 0.98, with a coefficient of variation (COV) of 0.12. These values indicate that the model made acceptable predictions of P_a' across all tests (including tests not in the training set). The mean actual-to-FE predicted deformation was 1.06, with a COV of 0.25. A better correlation is obtained for the rupture load (Fig. 10a) than the deformation (Fig. 10b) because displacements were small, and fracture typically occurred on the non-linear part of the load-deformation curve, as shown previously in Figs. 9a,b.

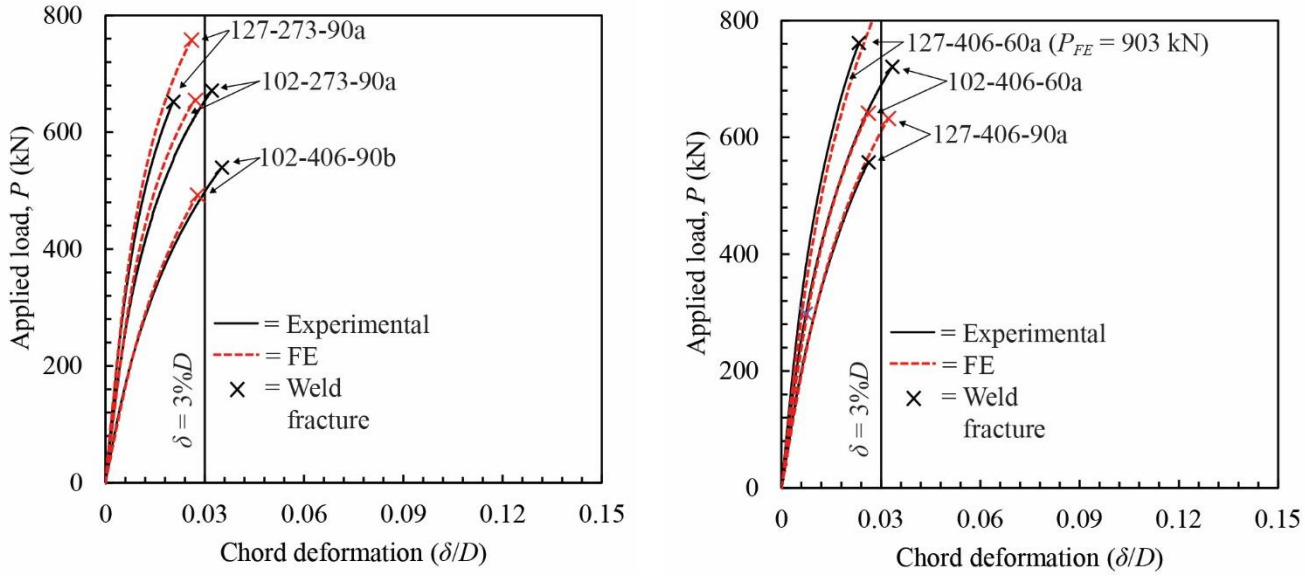

(a) Tests 102-273-90a, 102-406-90b, and 127-273-90a (b) Tests 127-406-90a, 102-406-60a, and 127-406-60a

Fig. 9. Comparison of experimental and FE load-deformation curves

244

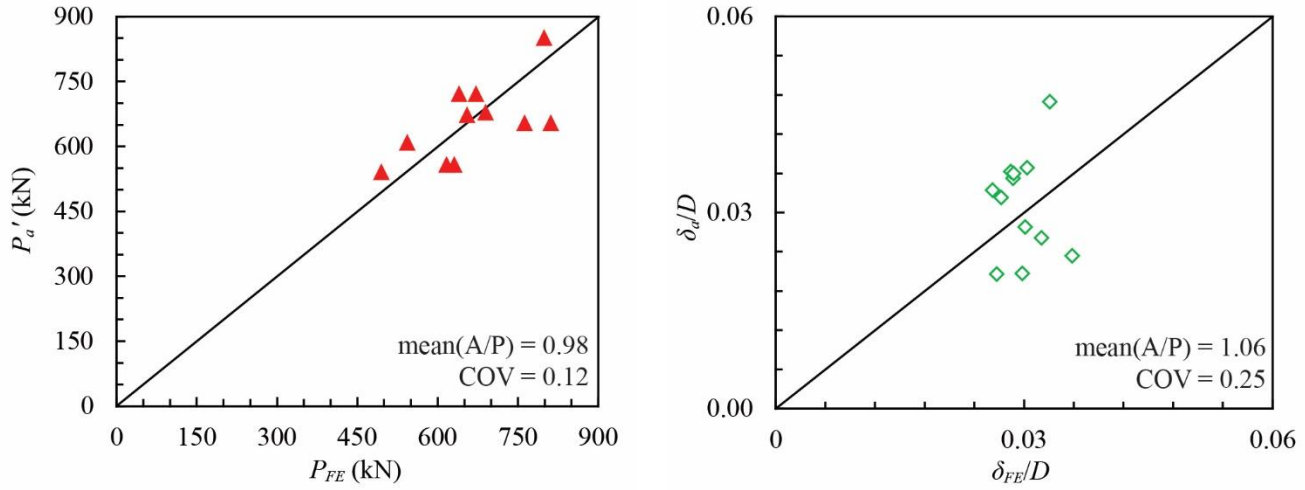

(a) Ultimate load (b) Chord deformation at rupture

Fig. 10. Correlation of experimental and FE results

245

246 In Fig. 10b, one point lies well above the line representing perfect correlation between the experimental and FE
247 chord deformation at rupture. The large difference for this test (102-406-90a) is not likely due to the influence of
248 any specific parameter (the difference for a similar test, 102-406-90b, was smaller) (Table 1). Given that both tests
249 had similar externally measured weld sizes, it is believed that the large difference is caused by excessive root
250 penetration, which was not explicitly taken into account in the FE models.

Experimental spot strain measurements from SGs located 20 mm from the weld (around one half of the weld, due to symmetry about the plane of the connection), oriented along the axis of the branch, indicated that elastic load transfer peaked at the saddle point of the connection (subtended angle, ρ = 90°) [1]. The sign convention for ρ is shown on Fig. 6b (clockwise from the heel). Typical measurements of elastic strain parallel to the branch along a line intersecting these gauges in the FE models (indicated by a dashed line in Fig. 6b) are shown in Figs. 11a,b. In Figs. 11a,b, elastic branch strains from experiments are represented by solid lines at an applied load (P) equal to $0.25P_a$ (i.e. 25% of the load at which the weld actually ruptured in the experiments, during the same monotonic loading phase), with the FE strains (solid red lines) predicting the same trends and values as shown by experimental strains. It is shown that the agreement between the FE and experimental strain distributions under elastic load (P = $0.25P_a$) was generally good. At ultimate (P = P_a), the FE strain distributions showed the same trend as the experimental strain distributions; however, they poorly predicted the experimental spot strain values. This is believed to be due to progressive and non-uniform yielding of the weld along its length, due to variations in the experimental weld geometry. These variations were not captured in the FE models. Nonetheless, the FE models: (a) provided further evidence that load peaked in the saddle position; and (b) revealed that weld rupture initiated in the saddle position (i.e. the first killed elements were at this location). After initial rupture in the FE models, failure propagated in both directions towards the crown points.

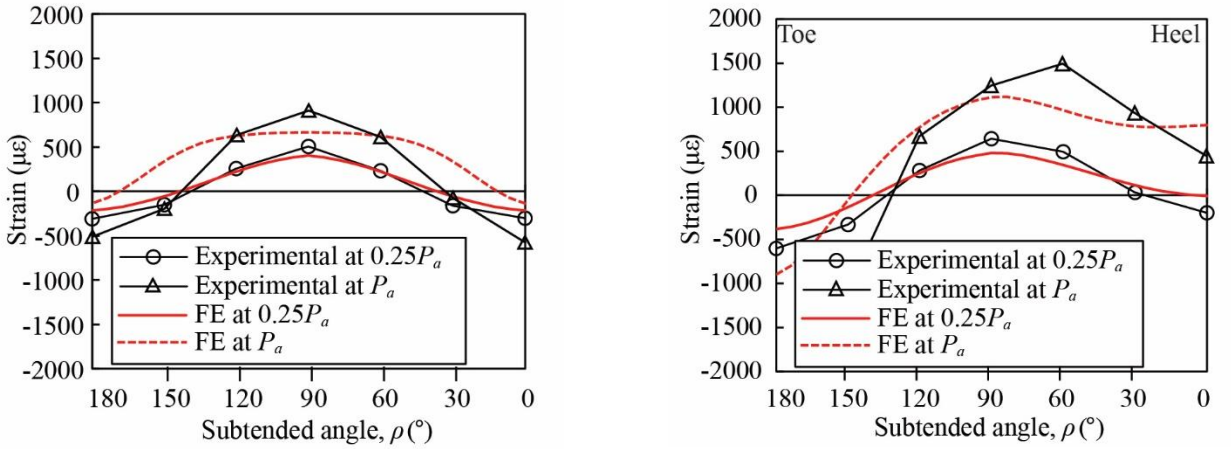

(a) Test 127-273-90a (β = 0.47, θ = 90°, τ = 0.99) (b) Test 102-406-60a (β = 0.25, θ = 60°, τ = 0.60)

Fig. 11. Comparison of typical experimental and FE longitudinal strain distributions adjacent to the weld

5. Finite element parametric study

For the parametric study, a range of non-dimensional connection parameters was chosen to cover all permissible fillet-welded connections subject to the following restrictions: (a) the local dihedral angle (Ψ) limits imposed by AWS [2] Fig. 9.10 and Table 9.5 ($60° \leq \Psi \leq 120°$); (b) the limits of applicability of connection design formulae in AISC [4] Table K3.1, which are given in AISC [4] Table K3.1A; and (c) the range of standard CHS sections available for designers in Table 1-13 of [20]. The parameters varied were: the branch inclination angle (θ = 60°, 70°, 80°, and 90°); the chord slenderness (D/t = 10, 20, 30, 40, and 50); the branch-to-chord dimeter ratio (β = 0.10, 0.20, 0.30, 0.40, and 0.50); and the branch-to-chord thickness ratio (τ = 0.20, 0.40, 0.60, 0.80, and 1.00). Although a total of 500 permutations exist for the values given, there are several practical limitations that must be considered. First, available CHS sections limit branch slenderness ratios (D_b/t_b) to between about 10 and 50. Secondly, not all combinations of β and θ produce Ψ between 60° and 120° along the entire weld length. Fig. 12 shows the results of a study conducted to determine compatible values of β and θ that meet this requirement. It is shown that permissible values of β range from 0.50 (for 90° connections) to 0.28 (for 60° connections).

A comprehensive parametric study was performed by modelling β up to 0.30 for 60° connections and β up to 0.50 for all other branch angles. A total of 256 CHS X-connection models was analyzed.

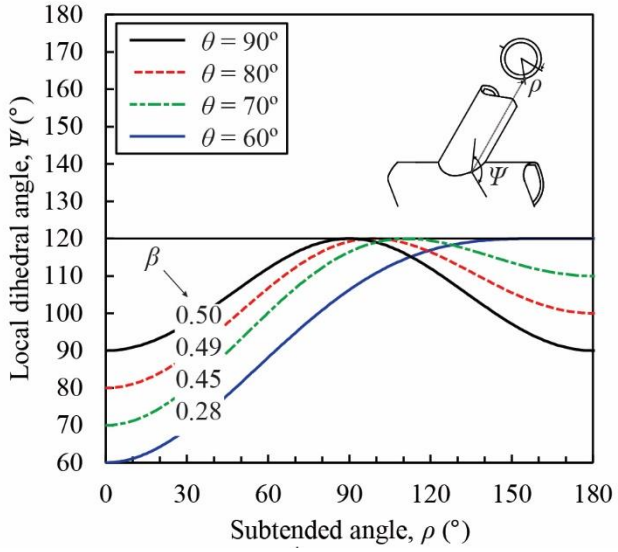

Fig. 12. Compatible values of β and θ to keep Ψ between 60° and 120° along the entire weld length, determined using methodology by Luyties & Post [21]

5.1. Details of parametric models

The parametric FE models had a constant branch diameter (D_b) of 200 mm. Although this is larger than D_b used in the experiments (Table 1), Section 3.2.2 demonstrated that the the normalized rupture load (P_{FE}/A_wF_{EXX}) remains largely unaffected. All models also contained an average weld throat dimension (t_w) equal to $0.50t_b$ to ensure that the branch yield capacity was not reached before weld fracture. As in the experiments, the ends of the chords were uncapped and unrestrained. The length of the chord (l) was $10D$ (when $D/t > 25$) or $6D$ (when $D/t \leq 25$) to prevent chord end effects at the connection [22]. The length of the branches (l_b) was $3D_b$, and load was applied to their ends. Load application was therefore in the theoretical constant stress region [23].

All models used the same set of material properties for the weld, the branches, and the chord. These material properties were based on materials tested experimentally that gave the most nominally matched weld metal and base metals. Fig. 13 shows the engineering stress-strain curves for these materials, which were converted to true-stress strain curves (see Section 3.1) for use in ANSYS. Table 4 summarizes the Young's modulus (E), yield stress (F_y), and ultimate stress (F_u, or F_{EXX} for weld metal) of these materials.

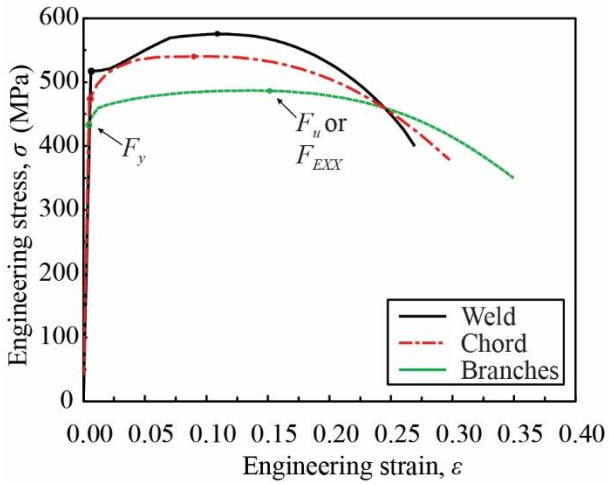

Fig. 13. Engineering stress-strain curves for materials used in the parametric models

Table 4
Young's modulus, yield stress and ultimate stress of materials used in the parametric models

	Young's modulus, E	Yield stress, F_y	Ultimate stress, F_u (or F_{EXX} for weld metal)
	MPa	MPa	MPa
Weld	208,000	517	577
Chord	208,000	460	540
Branches	191,200	431	488

Both welds were modelled as the same size, but the fracture criterion was only assigned to the upper (test) weld (e.g. as indicated previously in Figs. 3 and 4). The other weld, the branches, and the chord were not permitted to fracture. The model was loaded by applying uniform incremental displacements to the ends of each branch. The applied load (P) was obtained by summing up nodal forces parallel to the branch at the end of one branch, and multiplying by two to account for the half model. Chord deformation (δ) was obtained as described in Section 3.2, with the vertical displacement taken between nodes on two branches at 50 mm from the crown (Fig. 7a, shown previously). No axial load was applied to the chord.

6. Results and evaluation of the parametric study

All 256 FE analyses failed by weld fracture and the branches of the connections always remained elastic. Fracture initiated in the weld (evidenced by killed elements) at the saddle point ($\rho = 90°$ in Fig. 6b) and propagated away from the saddle towards the crown.

The FE chord deformation at weld rupture (δ_{FE}) was compared to the 3%D chord plastification limit, which is internationally accepted as a good estimator of the deformation-based capacity of ductile CHS connections [16]. The ratio of $\delta_{FE}/0.03D$ ranged from 0.10 to 2.58, and chord plastification ($\delta_{FE}/0.03D \geq 1$) was reached or surpassed in 97 out of the 256 FE tests. The weld sizes studied thus spanned a broad range of welded joint situations, from well below to well beyond "connection strength". Fig. 14 shows the relationship between δ, expressed as a fraction of the chord diameter (δ/D), and the applied load, normalized by the weld area and the electrode ultimate strength (P/A_wF_{EXX}), for typical tests. It is shown that deformation (δ/D) and strength (P/A_wF_{EXX}) varied widely across the FE tests at rupture.

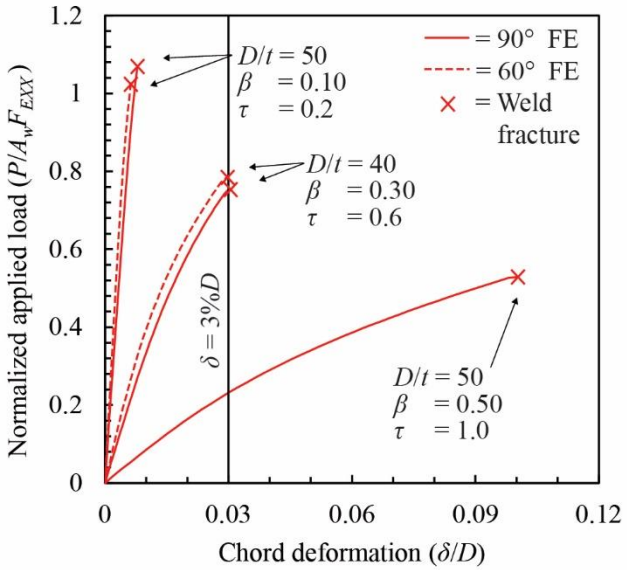

Fig. 14. Load-deformation curves for typical FE tests

To determine the weld effective length (l_e), first the strength of the fillet weld in each connection was predicted using Eq. (11), which was developed from regression of a large database of weld-critical CHS-to-rigid end-plate connection FE analysis results, in which the welds were fully effective [19]:

$$P_n = \left(1.009 - 0.00137\frac{D_b}{t_b} - 0.197\frac{t_w}{t_b}\right) A_w F_{EXX} \tag{11}$$

Eq. (11) is tailored to the unique loading on single-sided fillet welds to CHS branches (which produces tension at the weld root under branch axial tension), and takes into account the principal influential geometric parameters of the CHS member and weld joint on the strength of fillet welds.

The fraction of the weld length that is effective (l_e/l_w) in the CHS-to-CHS joint was then determined by dividing the weld FE strength by the predicted weld strength from Eq. (11). This method for determining the weld effective length in CHS-to-CHS X-connections was deemed appropriate in [1].

Determined in this manner, 138 (out of 256) FE connections had weld effective lengths less than 1.0. The smallest weld effective length was 0.58 times the total weld length (for D/t = 50, β = 0.50, τ = 1.0 and θ = 80°), and the largest weld effective length was 1.22 times the total weld length (for D/t = 50, β = 0.10, τ = 0.2 and θ = 90°). The fact that weld effective lengths were sometimes greater than 1.0 is believed to be due, in part, to the scatter

associated with the best-fit prediction equation [Eq. (11)], and also due to the effect of secondary forces on the weld due to local bending of the chord.

6.1. Effect of chord slenderness and branch-to-chord diameter ratio

As D/t increases, CHS X-connections become more flexible, due to a decrease in bending stiffness of the chord wall. Chord deformations at rupture become larger, and calculated weld effective lengths at rupture are generally smaller. Fig. 15a shows the relationship between the calculated weld effective length, expressed as a fraction of the total weld length (l_e/l_w) and D/t. Fig. 15b shows the relationship between l_e/l_w and β. Fig. 16 shows the relationship between l_e/l_w and the product $(D/t)\beta$. For clarity, the results have been shown as mean values with ± one standard deviation bars. Smaller scatter bars indicate a more statistically significant correlation between l_e/l_w and the independent variable. It can be seen that the quantity $(D/t)\beta$ has a strong correlation to l_e/l_w. For values of $(D/t)\beta$ greater than approximately eight, this relationship resembles a power law. For values of $(D/t)\beta$ less than or equal to eight, l_e/l_w plateaus (at a value greater than 1).

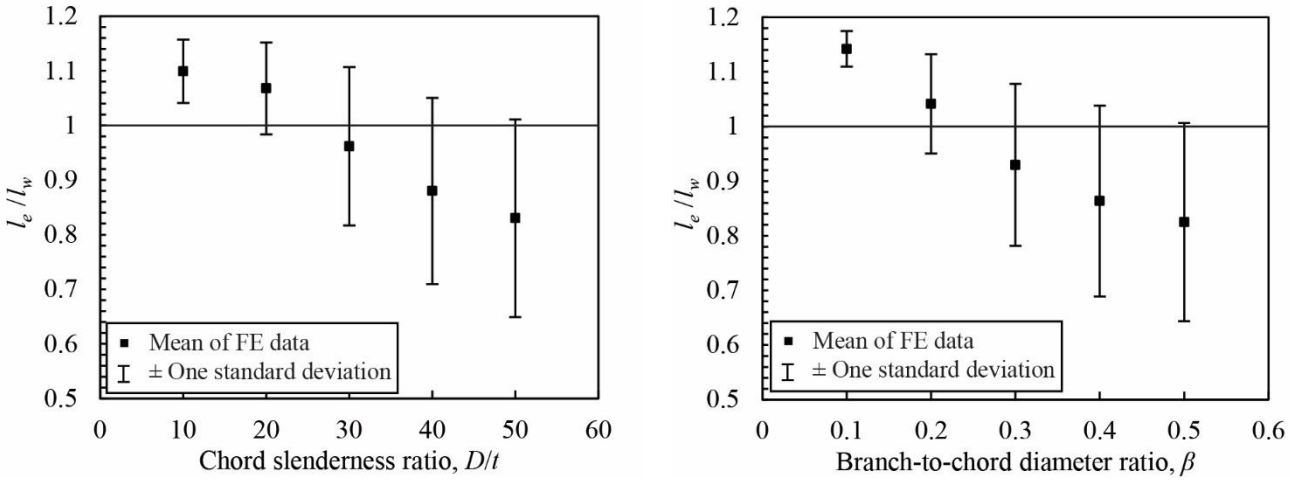

(a) chord slenderness (b) branch-to-chord diameter ratio

Fig. 15. Effect of chord slenderness and branch-to-chord diameter ratio on effective length

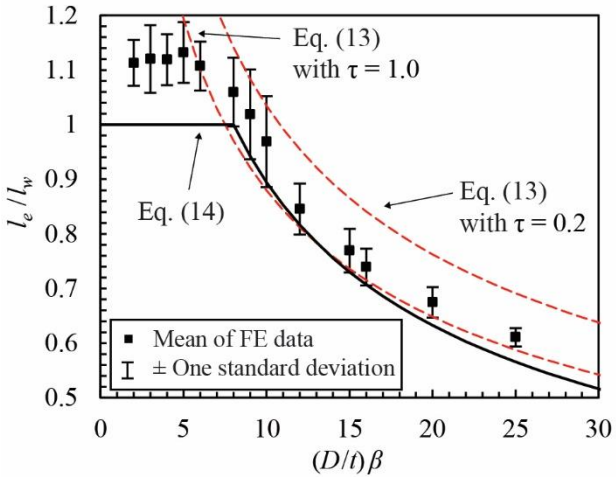

Fig. 16. Effect of the product $(D/t)\beta$ on effective length

347

348 *6.2. Effect of branch inclination angle*

349 Fig. 17 shows the relationship between θ and l_e/l_w for connections with β = 0.10, 0.20 and 0.30, since
350 connections with $\theta = 60°$ were only tested for β up to 0.30. Fig. 17 indicates a marginal decrease in l_e/l_w as θ increases
351 from 60° to 90°. The change in mean value over this range is only 3.5%. Overlapping of the ± one standard deviation
352 bars for all points indicates that the effect of θ is not statistically significant. This is also indicated by the similar
353 load-deformation curves in Fig. 14 for connections with θ = 60° and 90° and all other parameters constant. The
354 branch inclination angle is thus found to have no effect.

355

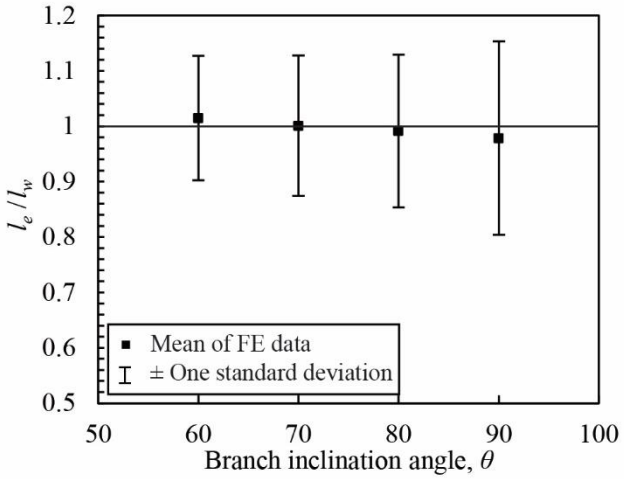

Fig. 17. Effect of branch inclination angle on effective length

356

357 *6.3. Effect of branch-to-chord thickness ratio*

358 As τ increased in the experimental tests, more non-uniform strain distributions, similar to the elastic strain
359 distributions, were observed at rupture, and the average weld strength (P_a'/A_wF_{EXX}) was generally lower [1]. Fig. 18
360 shows the relationship between τ and l_e/l_w for the FE tests. As τ increases from 0.2 to 1.0, the average value of l_e/l_w
361 decreases. The relationship is approximately linear.

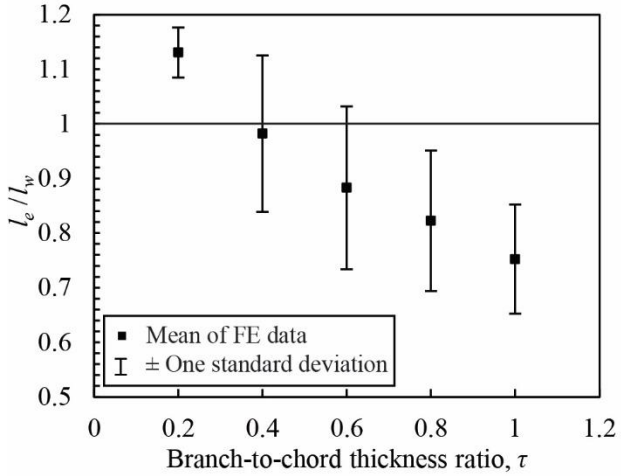

Fig. 18. Effect of branch-to-chord thickness ratio on effective length

362

363 **7. Regression analysis**

364 A non-linear regression analysis was performed with Eq. (12) as a basis:

$$\frac{l_e}{l_w} = \frac{C}{\tau^b(\beta\gamma)^a} \quad (12)$$

where a, b, and C = regression constants, and γ = half-diameter-to-thickness ratio of the CHS chord (= $D/2t$). The half-diameter-to thickness-ratio of the CHS chord is a standard parameter for HSS connection design.

The arrangement of variables in Eq. (12) was determined empirically, with efforts made to take into account the relationships discussed in Section 6. The values of a, b, and C were determined by least-squares regression of the 138 FE results with $l_e/l_w < 1$, since above this value the relationship changes, and it is inapplicable for design. The "best-fit" equation is given by Eq. (13):

$$\frac{l_e}{l_w} = \frac{1.786}{\tau^{0.1007}(\beta\gamma)^{0.440}} \quad (13)$$

Eq. (13) gives a mean value of actual-to-predicted rupture strength of 1.001 over the 138 tests with a COV of 0.030. Eq. (13) with τ = 0.2 and Eq. (13) with τ = 1.0 are plotted as dashed lines on Fig. 16. These two curves represent the extremes of the τ data, and also show that Eq. (12) as a basis for the regression is appropriate because it describes the predominant data trends. For a lower-bound to Eq. (13), the value of τ can be taken as 1.0 (the maximum τ in this study and a recommended maximum in practice) which is synonymous with taking b equal to zero in Eq. (12). Eq. (14) is proposed as an even simpler equation for determining the weld effective length (l_e) as a ratio of the total weld length in CHS X-connections:

$$\frac{l_e}{l_w} = \frac{2}{\sqrt{\beta\gamma}} \leq 1 \quad (14)$$

Eq. (14) is plotted as a solid line in Fig. 16. It implies that weld effective lengths do not exist in CHS X-connections when $\beta\gamma \leq 4$. Eq. (14), plotted in Fig. 19, embodies the trend established by Caulkins [9] and Marshall [10] for the range of β and D/t in this study ($0.10 \leq \beta \leq 0.50$ and $10 \leq D/t \leq 50$). As β and D/t increase, the load transfer efficiency (or for this study, l_e/l_w) decreases. The rate of decrease is greater for lower values of β and D/t, when $\beta\gamma > 4$.

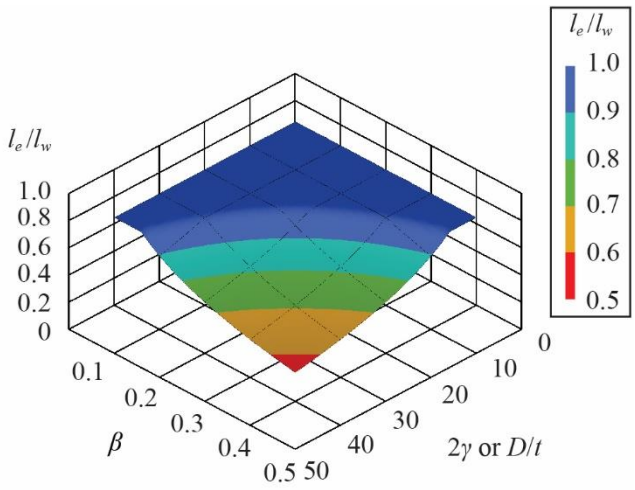

Fig. 19. Weld effective lengths in CHS-to-CHS X-connections with $0.10 \le \beta \le 0.50$ and $10 \le D/t \le 50$ according to Eq. (14)

8. Evaluation of design methods

8.1. Fit-for-purpose design methods for fillet welds

The nominal strength (P_n) of fillet welds in CHS X-connections designed as fit-for-purpose is generally given by:

$$P_n = F_{nw} t_w l_e \tag{15}$$

where F_{nw} = nominal weld strength. An LRFD resistance factor for fillet welds, ϕ, is then applied to determine ϕP_n. Note that Eqs. (1) and (2) can be written in this form.

8.1.1. Proposed procedure

Step 1) Calculate F_{nw} using $(1 - 0.25P_r/P_y)$, where P_r = required strength of the weld and P_y = branch yield load (= $A_b F_y$). This equation is a simplification of Eq. (11), and is based on fillet-welded CHS-to-rigid end-plate experimental and FE research [19] in which the total weld length is effective.

Step 2) Determine the total weld length (l_w) by an acceptable means (e.g. AWS [2] Clause 9.5.4, or CAD).

Step 3) Determine the ratio l_e/l_w using Eq. (14).

Step 4) Calculate l_e by multiplying the results of Steps 2) and 3).

Step 5) Calculate P_n using Eq. (15), for a given value of t_w.

Step 6) Apply the appropriate ϕ value to determine ϕP_n for design.

8.1.2. Safety level inherent in proposed procedure

To verify that an adequate safety margin is inherent in the above recommendation, the structural reliability (or safety index) (β^+) can be calculated using a reliability analysis in which the resistance factor, ϕ, is given by Eq. (16) [24,25]:

$$\phi = \phi_{\beta^+}\rho_R \exp\left[-\alpha_R \beta^+ V_R\right] \tag{16}$$

where α_R = coefficient of separation taken as 0.55 [24]; ρ_R = bias coefficient for resistance; V_R = associated coefficient of variation (COV) of ρ_R; and ϕ_{β^+} = adjustment factor for β^+ that is needed when $\beta^+ \neq 3.0$ [25]. The bias coefficient for resistance (ρ_R) and its associated COV (V_R) are given by Eqs. (17) and (18):

$$\rho_R = \rho_M \rho_G \rho_P \tag{17}$$

$$V_R = \sqrt{V_M^2 + V_G^2 + V_P^2} \tag{18}$$

where ρ_M = mean ratio of actual-to-nominal electrode strength; ρ_G = mean ratio of actual-to-nominal weld throat area; ρ_P = mean test-to-predicted capacity ratio (with predicted capacity calculated using actual measured properties); and V_M, V_G, and V_P are COVs of ρ_M, ρ_G, and ρ_P, respectively.

The mean test-to-predicted capacity ratio (ρ_P) was taken as the average over all experimental and FE tests of P_a' (or P_{FE}) calculated using Steps 1) - 5), using measured (or actual) values of t_w and F_{EXX}. In Step 1), P_r was taken as P_a' or P_{FE} for a worst-case scenario. The total weld length (l_w) was determined using a highly accurate vector-calculus approach described in [1]. The same values or equations used in [1] for the other reliability analysis parameters (ρ_M, ρ_G, ρ_P, V_M, V_G, V_P, and ϕ_{β^+}) have also been used herein (Table 5). A total of 268 tests (12 experimental plus 256 FE) were included in the reliability analysis.

Table 5 gives the results of the reliability analysis using three different values of ϕ. The safety indices calculated for the proposed design method for each value of ϕ can be compared to target values given in the United States (β^+ = 4.0, per Section B3.1 of the AISC [4] Commentary) and Canada (β^+ = 4.5, per Annex B of CSA [5]).

Table 5

Reliability analysis parameters for proposed procedure with ϕ = 0.80, 0.75 and 0.67

ϕ [a]	0.80	0.75	0.67
ρ_M	1.12	1.12	1.12
V_M	0.12	0.12	0.12
ρ_G	1.03	1.03	1.03
V_G	0.10	0.10	0.10
ρ_P	1.12	1.12	1.12
V_P	0.08	0.08	0.08
ρ_R	1.29	1.29	1.29
V_R	0.18	0.18	0.18
$\phi_{\beta}{}^{+}$	0.91	0.89	0.84
β^{+}	4.0	4.3	5.0

[a] resistance factors for fillet welds according to AWS [2], AISC [4], and CSA [5] (see [1]).

The implied safety index (β^{+}) is ≥ 4.0 when ϕ = 0.80 (as used by AWS [2]). Furthermore, β^{+} is ≥ 4.0 when ϕ = 0.75 (as used by AISC [4]), and β^{+} is ≥ 4.5 when ϕ = 0.67 (as used by CSA [5]). This indicates that the method meets U.S. and Canadian safety indices. Fig. 20 shows the correlation of the predicted nominal strengths using Steps 1) – 5) for the proposed procedure with the experimental and FE results. On average, the test capacity is only 1.12 times larger than the predicted rupture load, with a COV of 0.08.

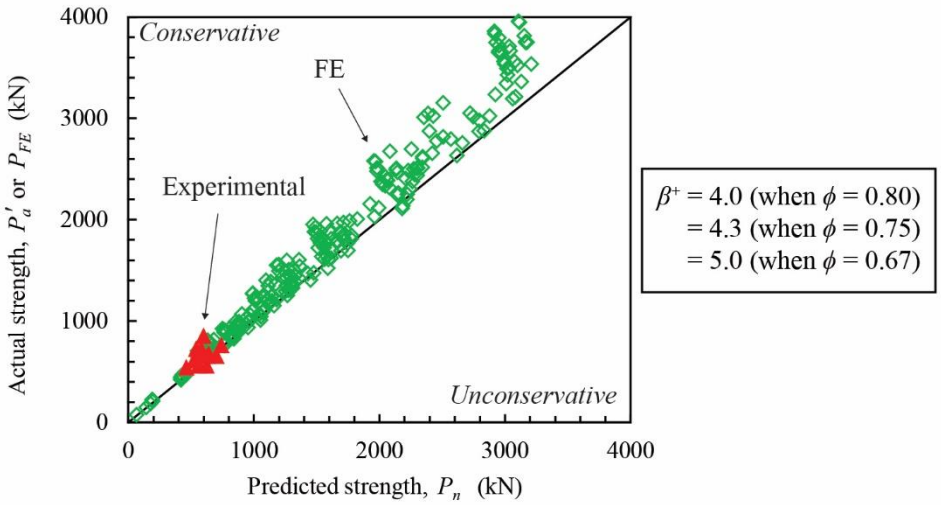

Fig. 20. Correlation of proposed design method with all test results

8.1.3. Safety level inherent in AWS [2], AISC [4] and CSA [5]

The reliability analysis was repeated, using all 268 numerical and FE tests, to determine the implied safety index, β^{+}, for the current AWS [2] provisions, with and without the (2/3)l_w weld effective length factor, and the AISC [4] and CSA [5] provisions, as presented in Tousignant & Packer [1]. The analysis determined that β^{+} = 6.2

437 ≥ 4.0 for AWS [2] with $l_e = (2/3)l_w$, $\beta^+ = 4.3 \geq 4.0$ for AWS [2] with $l_e = l_w$, and $\beta^+ = 4.6$ for both AISC [4] and CSA
438 [5] > 4.0 and 4.5. It can therefore still be concluded that weld effective lengths are never required for fillet-welded
439 CHS X-connections in conjunction with these code design methods. The mean test-to-predicted capacity ratio (ρ_P)
440 and V_p for these methods ($\rho_P = 2.07$ for AWS [2] with weld effective lengths, $\rho_P = 1.38$ for AWS [2] without weld
441 effective lengths and AISC [4], $\rho_P = 1.24$ for CSA [5], and $V_p = 0.19$ for all methods) indicate that the proposed
442 procedure (Section 8.1.1) is much more accurate (ρ_P in Table 5 closer to 1) and precise (V_P in Table 5 closer to 0)
443 than the code methods for predicting fillet weld strength in CHS X-connections.

444 ## 9. Conclusions

445 Non-linear FE models with weld fracture were developed for fillet-welded CHS X-connections. These models
446 were validated by comparison with 12 weld-critical tests on CHS X-connections. A parametric study was then
447 performed in which 256 FE models with $60° \leq \theta \leq 90°$, $10 \leq D/t \leq 50$, $0.10 \leq \beta \leq 0.50$, and $0.20 \leq \tau \leq 1.00$ were
448 analysed. All models were shown to fail by weld fracture. Based on the parametric study, the following can be
449 concluded:

450 1. The weld effective length in CHS X-connections decreases as the branch slenderness (D/t), branch-to-chord
451 dimeter ratio (β), and branch-to-chord thickness ratio (τ) increase.
452 2. The branch inclination angle θ has an insignificant effect on the weld effective length.
453 3. Theoretically, the weld effective length can be as low as 0.58 times the total weld length.
454 4. The weld is 100% effective for $\beta\gamma \leq 4$.
455 5. For CHS X-connections load transfer peaks at the saddle position.
456 6. Stress re-distribution occurs prior to weld rupture, even in connections with small welds.

457 Based on a reliability analysis to determine the safety index (β^+) for 268 experimental and FE tests covering
458 the same range of parameters, the following can also be concluded:

459 7. The existing AWS [2] specification provisions for fillet welds in CHS X-connections in Clause 9.6.1.3(4),
460 with $l_e = (2/3)l_w$, are very conservative (safety index, $\beta^+ = 6.2 > 4.0$).
461 8. The existing AWS [2] specification provisions for fillet welds in CHS X-connections in Clause 9.6.1.3(4),
462 with $l_e = l_w$, are also conservative (safety index, $\beta^+ = 4.3 > 4.0$).

9. The existing AISC [4] provisions in Clause J2.4a and the existing CSA [5] provisions in Clause 13.13.2.2, with $l_e = l_w$, are conservative (safety index, $\beta^+ = 4.6$ for both > 4.0 and 4.5).

The evaluations of AWS, AISC and CSA fillet weld design provisions assume that the $(1+0.50\sin^{1.5}\theta)$ directional strength-enhancement factor is not used (AWS [2] Clause 2.6.4.2, AISC [4] Clause J2.4b, and CSA [5] Clause 13.13.2.2), because it has been shown to be generally unsafe for the design of fillet welds in HSS connections [26].

An alternative method for the design of fillet welds, based on rational weld effective lengths as a function of non-dimensional connection parameters, was proposed. This method was shown be more accurate and precise for predicting fillet weld strength in CHS X-connections than AWS [2], AISC [4] and CSA [5]. A reliability analysis with respect to all experimental and FE tests showed that this proposed method provides an adequate level of safety for use with AWS, AISC and CSA codes.

Acknowledgement

The authors gratefully acknowledge the Natural Sciences and Engineering Research Council of Canada (NSERC) for its financial support.

Notation

A_w	weld throat area (= $t_w l_w$)
A_b	cross-sectional area of the branch
D	diameter of the chord
D_b	diameter of the branch
E	Young's modulus
F_{EXX}	ultimate strength of weld metal
F_{nw}	nominal weld strength
F_u	ultimate strength of CHS
F_y	yield strength
K_a	weld length factor

490	P	applied load
491	$P_{3\%D,a}$	actual (experimental) load at connection plastification limit
492	$P_{3\%D,FE}$	finite element load at connection plastification limit
493	P_a	actual (experimental) weld fracture load
494	P_a'	greatest load sustained by the weld
495	P_{FE}	finite element weld fracture load
496	P_n	nominal predicted weld fracture load
497	P_r	required strength of the weld
498	P_y	yield load of the branch (= A_bF_y)
499	Q_w	shear strength of weld per unit length
500	V_G	coefficient of variation of ρ_G
501	V_M	coefficient of variation of ρ_M
502	V_P	coefficient of variation of ρ_P
503	V_R	coefficient of variation of ρ_R
504	a, b and C	regression constants
505	k_a	actual (experimental) initial stiffness
506	k_{FE}	finite element initial stiffness
507	l	length of the chord
508	l_b	length of the branch
509	l_e	weld effective length
510	l_h	weld leg along the chord
511	l_v	weld leg along the branch
512	l_w	total length of weld
513	t	thickness of the chord
514	t_b	thickness of the branch
515	t_w	weld throat dimension
516	w	weighting factor

517	α	chord length parameter (= $2l/D$)
518	α_R	coefficient of separation
519	β	branch-to-chord diameter ratio
520	β^+	safety index
521	γ	half diameter-to-thickness ratio of the chord
522	ε	engineering strain
523	ε_{ef}	equivalent strain fracture criterion
524	ε_T	true strain
525	ε_T'	true strain at the start of necking
526	δ	chord deformation
527	δ_a	actual (experimental) chord deformation at rupture
528	δ_{FE}	finite element chord deformation at rupture
529	ρ	subtended angle around the branch, measured clockwise from heel
530	ρ_G	mean ratio of measured-to-nominal weld throat area
531	ρ_M	mean ratio of measured-to-nominal electrode ultimate strength
532	ρ_P	mean test-to-predicted capacity ratio
533	ρ_R	bias coefficient for resistance
534	σ	engineering stress
535	σ_T	true stress
536	σ_T'	true stress at the start of necking
537	τ	branch-to-chord thickness ratio
538	ϕ	LRFD resistance factor for fillet welds
539	ϕ_{β^+}	adjustment factor for β^+
540	θ	branch inclination angle
541	Ψ	local dihedral angle
542		
543		

References

[1] Tousignant, K. & Packer, J. A. 2017. Fillet weld effective lengths in CHS X-connections. I: Experiments. *Journal of Constructional Steel Research* 138: 420-431.

[2] American Welding Society (AWS) 2015. AWS D1.1/D1.1M:2015. Structural welding code—steel. Miami, FL, USA.

[3] ISO (International Organization for Standardization). 2013. ISO 14346:2013 (E). Static design procedure for welded hollow section joints – Recommendations, Geneva, Switzerland.

[4] American Institute of Steel Construction (AISC) 2016. ANSI/AISC 360-16. Specification for structural steel buildings. Chicago, IL, USA.

[5] Canadian Standards Association (CSA) 2014. CSA S16-14. Design of steel structures. Toronto, Canada.

[6] Wardenier, J., Kurobane, Y., Packer, J. A., van der Vegte, G. J., & Zhao, X.-L. 2008. Design guide for circular hollow section (CHS) joints under predominantly static loading, CIDECT Design Guide No. 1, 2nd ed. Geneva, Switzerland: CIDECT.

[7] Comité Européen de Normalisation (CEN). 2005. EN 1993-1-8:2005. Eurocode 3: Design of steel structures – part 1-8: design of joints. Brussels, Belgium.

[8] Fleischer, O. & Herion, S. 2015. Reduction of fillet weld sizes. In Eduardo Batista, Pedro Vellasco and Luciano Lima (eds.), *Tubular Structures XV; Proc. Intern. Symp., Rio de Janeiro 27-29 May 2015.* Rotterdam: Balkema, 473-480.

[9] Caulkins, D. W. 1968. CDG Report 15. Parameter study for FRAMETI elastic stress in tubular joints. Houston, TX, USA: Shell Oil Company.

[10] Marshall, P.W. 1992. Design of welded tubular connections – Basis and use of AWS code provisions. Amsterdam, The Netherlands: Elsevier.

[11] Wang, W., Gu, Q., Ma, X. & Wang, J. 2015. Axial tensile behavior of welds for CHS branches to SHS chord joints. *Journal of Constructional Steel Research* 115: 303-315.

[12] Swanson Analysis Systems. 2011. ANSYS ver. 14.0. Houston, TX, USA.

[13] ASTM International 2017. ASTM A370-17. Standard test methods and definitions for mechanical testing of steel products. West Conshohocken, PA, USA.

[14] Boresi, A. P. & Schmidt, R. J. 2003. Advanced mechanics of materials, 6th ed. New Jersey, USA: John Wiley and Sons, Inc.

[15] Ling, Y. 1996. Uniaxial true stress-strain after necking. *AMP Journal of Technology* 5(1): 37-48.

[16] Lu, L. H., de Winkel, G. D., Yu, Y. & Wardenier, J. 1994. Deformation limit for the ultimate strength of hollow section joints. In Paul Grundy, Alan Holgate and Bill Wong (eds.), *Tubular Structures VI; Proc. Intern. Symp., Melbourne 14-16 December 1994.* Rotterdam: Balkema, 341-348.

[17] Martinez-Saucedo, G., Packer, J. A. & Willibald, S. 2006. Parametric finite element study of slotted end connections to circular hollow sections. *Engineering Structures* 28(14): 1956-1971.

[18] Voth, A. P. and Packer, J. A. 2012. Branch plate-to-circular hollow structural section connections. I: Experimental investigation and finite-element modeling. *Journal of Structural Engineering, American Society of Civil Engineers* 138(8): 995-1006.

[19] Tousignant, K. & Packer, J. A. 2017. Numerical investigation of fillet welds in HSS-to-rigid end-plate connections. *Journal of Structural Engineering, American Society of Civil Engineers* 143(12): 04017165-1 – 04017165-16.

[20] American Institute of Steel Construction (AISC) 2010. Steel construction manual, 14th ed. Chicago, IL, USA.

[21] Luyties, W. H. & Post, J. W. 1988. Local dihedral angle equations for tubular joints and related applications. *Welding Journal* 77(4): 51-60.

[22] van der Vegte, G.J. & Makino, Y. 2010. Further research on chord length and boundary conditions of CHS T- and X-joints. *Advanced Steel Construction* 6(3): 879-890.

[23] Mehrotra, B. L. & Govil, A. K. 1972. Shear lag analaysis of rectangular full-width tube connections. *Journal of the Structural Division, American Society of Civil Engineers* 98(ST1): 287-305.

[24] Ravindra, M. K. & Galambos, T. V. 1978. Load and resistance factor design for steel. *Journal of the Structural Division, American Society of Civil Engineers* 104(9): 1337-1353.

[25] Fisher, J. W., Galambos, T. V., Kulak, G. L. & Ravindra, M. K. (1978). Load and resistance factor design criteria for connectors. *Journal of the Structural Division, American Society of Civil Engineers* 104(9): 1427-1441.

598 [26] Packer, J. A., Sun, M., & Tousignant, K. 2016. Experimental evaluation of design procedures for fillet
599 welds to hollow structural sections. *Journal of Structural Engineering, American Society of Civil Engineers*
600 142(5): 04016007-1 – 04016007-12.

Figure Captions

Fig. 1. CHS X-connection general configuration and non-dimensional parameters

Fig. 2. Load transfer efficiency across the weld of a 90° CHS-to-CHS T-connection (adapted from Marshall [10])

Fig. 3. FE CHS-to-CHS X-connection geometry, mesh layout, and boundary conditions with $\theta = 90°$

Fig. 4. FE CHS-to-CHS X-connection geometry, mesh layout, and boundary conditions with $\theta < 90°$ ($\theta = 60°$ shown)

Fig. 5. Comparison of typical experimental (solid line) and FE (dashed line) stress-strain curves

Fig. 6. Mesh layouts used in the mesh sensitivity study

Fig. 7. Comparison of FE and experimental mesh sensitivity parameters for test 102-273-90a

Fig. 8. Ratios of P_a'/P_{FE} and δ_a/δ_{FE} for the training set for different values of ε_{ef}

Fig. 9. Comparison of experimental and FE load-deformation curves

Fig. 10. Correlation of experimental and FE results

Fig. 11. Comparison of typical experimental and FE longitudinal strain distributions adjacent to the weld

Fig. 12. Compatible values of β and θ to keep Ψ between 60° and 120° along the entire weld length, determined using methodology by Luyties & Post [21]

Fig. 13. Engineering stress-strain curves for materials used in the parametric models

Fig. 14. Load-deformation curves for typical FE tests

Fig. 15. Effect of chord slenderness and branch-to-chord diameter ratio on effective length

Fig. 16. Effect of the product $(D/t)\beta$ on effective length

Fig. 17. Effect of branch inclination angle on effective length

Fig. 18. Effect of branch-to-chord thickness ratio on effective length

Fig. 19. Weld effective lengths in CHS-to-CHS X-connections with $0.10 \leq \beta \leq 0.50$ and $10 \leq D/t \leq 50$ according to Eq. (14)

Fig. 20. Correlation of proposed design method with all test results